Angle-resolved resonant inelastic x-ray scattering from transition-metal magnetic ions

P. Ferriani,* C. M. Bertoni, and G. Ferrari
INFM, National Research Center on Nanostructures and Biosystems at Surfaces (S^3) *and Dipartimento di Fisica, Università di Modena e Reggio Emilia, Via Campi 213/A, 41100 Modena, Italy*

(Received 2 September 2003; revised manuscript received 18 November 2003; published 30 March 2004)

We present a study on the x-ray inelastic scattering at the $2p$ resonance of transition metals. The theoretical results are discussed in the single-ion model with crystal-field corrections and the full description of multiplet manifolds. The interference effects among the intermediate states are described as a function of the directions and polarizations of the incoming and outcoming beams. We consider the special case where the emission is due to inner-shell recombination. A variety of peculiar effects are discussed, with special reference to the perpendicular geometry of the incoming beam. The simplest cases are analytically examined showing the potential sensitivity of this technique to the electronic structure. Numerical results for the total and dichroic signals for some elements of the $3d$ series are given.

DOI: 10.1103/PhysRevB.69.104433 PACS number(s): 75.25.+z, 75.50.−y, 78.70.Ck

I. INTRODUCTION

Thanks to the technical progress of synchrotron-radiation sources in recent years resonant inelastic x-ray scattering[1] (RIXS) has become a powerful technique of increasing interest for the study of electronic and magnetic properties of solids. The higher selectivity with respect to x-ray absorption spectroscopy (XAS), due to the possible choice of the deexcitation channel and the propagation direction of the outgoing photons, allows one to obtain information not accessible in XAS. In fact, the study of the angular distribution of the emitted photons allows one to recover: (i) information on the core hole created in the absorption step;[2] (ii) the multipole moments (even of higher order) of the charge and magnetic densities of the partially filled shells in the atomic ground state, through the use of sum rules that have been developed theoretically in the last decade.[3–6] A similar description can be provided for the other resonant process, where the deexcitation channel is given by the Auger effect.[7]

RIXS can be a tool of the investigation of the electronic and magnetic properties at the atomic scale for the understanding of many hot topics in condensed-matter physics of recent years (giant magnetoresistance, magnetic anisotropy, interlayer coupling, and so on). To this aim, it is particularly interesting to study the perpendicular geometry,[8] where the incident beam impinges orthogonally with respect to the magnetization. In this configuration XAS shows no magnetic dichroism, while a dichroic signal can be detected in RIXS.[9–12] Its origin is linked to the creation of a polarized core hole in the absorption step and it is detectable only in presence of a nonvanishing projection of the emission direction along the sample magnetization.[8,9] The perpendicular geometry is convenient for a simpler and straightforward application of the sum rules[13] as well as for bypassing some experimental difficulties.[14]

For these reasons the study of the angle and polarization dependence of the RIXS cross section has become of paramount importance. A convenient formalism was developed by Fukui *et al.*,[11,12] in the case when the magnetization belongs to the scattering plane, showing the crucial role of the interference among the states of the intermediate configuration of the process to account for dichroism in the perpendicular geometry.

A recent demonstration by Braicovich *et al.*[15] of the feasibility of the quantitative recovery of the multipole moments up to order 4 (presented for cobalt ions in $CoFe_2O_4$), adopting a particular geometry where the magnetization and the incident and emitted beam do not belong to the same plane, suggests the extension of the previous results to include such more general case.

We consider here the scattering process involving the transitions $2p^6 3d^n \rightarrow 2p^5 3d^{n+1} \rightarrow 2p^6 3s^1 3d^{n+1}$. The scattering is deeply inelastic, thus the feasible experiment can avoid self-absorption problems. Anyhow the same formalism can be applied to the case of quasi-elastic scattering $2p^6 3d^n \rightarrow 2p^5 3d^{n+1} \rightarrow 2p^6 3d^n$, involving the same multiplets in the initial and final configurations.

In this paper the expression for the angle-dependent cross section in the dipole-dipole channel is given in the most general geometrical setup, both for the total value summed on the two incoming beam polarization and for the circular dichroism. It is written as an explicit function of the angles defining the directions of the incoming and outgoing beams, so that it can be directly used for the comparison with experiments. The case where the propagation direction of the emitted photon is out of the plane defined by the direction of the incident photon and the sample magnetization is investigated in detail, highlighting the importance of the interference among the intermediate states for the description of the angular dependence. In this case an asymmetry for emission with respect to that plane is found. Its origin is linked to the presence of the magnetization. Particular relevance is given to the perpendicular geometry, where numerical calculations performed for the L_3 threshold of some $3d$ transition metal (TM) systems are supplied. The pedagogical case of the Ni^{2+} in cylindrical symmetry is discussed following step by step the calculations.

The paper is organized as follows. In Sec. II the angle-resolved differential cross section is given; in Sec. III the role of the interference between the states of the intermediate configuration is pointed out; the details of the numerical approach are given in Sec. IV, together with the discussion on

crystal-field and finite-temperature effects; numerical calculations for Mn^{2+}, Co^{2+}, and Ni^{2+} are shown and discussed in Sec. V, after a presentation of the simple case of the Ni^{2+} in SO_2 symmetry which can be analytically examined; Sec. VI is devoted to the conclusions.

II. ANGLE- AND POLARIZATION-RESOLVED DIFFERENTIAL CROSS SECTION

The scattering cross section in resonant condition is given by[16]

$$\frac{d^2\sigma}{d\Omega' d(\hbar\omega')} = \sum_{|f\rangle} \left| \sum_{|n\rangle} \frac{\langle f|T^{(e)}|n\rangle\langle n|T^{(a)}|i\rangle}{E_i - E_n + \hbar\omega + i\frac{\Gamma_n}{2}} \right|^2 \times \delta(E_i - E_f + \hbar(\omega - \omega')), \quad (1)$$

where we have omitted the multiplicative constants and the very slow varying factor (ω'/ω), unimportant at the $2p$ threshold in TM's. It represents the rate of emission of photons of energy $\hbar\omega'$ in the solid angle $d\Omega'$ centered in the emission direction, after the excitation of the system with photons of energy $\hbar\omega$. $|i\rangle$, $|n\rangle$, and $|f\rangle$ are the initial, intermediate, and final states of the process with energies E_i, E_n, and E_f respectively; the δ function accounts for the energy conservation. $T^{(a)}$ and $T^{(e)}$ are the transition operators for the incident and emitted photons, respectively. Γ_n, the intrinsic linewidth connected with the finite lifetime of the intermediate state $|n\rangle$, prevents the divergence of the cross section at resonance. The presence of a complex energy $E_n - i(\Gamma_n/2)$ in the denominator is equivalent to the inclusion of higher-order terms of the interaction into the second-order perturbation expansion.[17]

The explicit forms of the transition operators, for the case of dipolar excitation and decay involved in the $L_{2,3}$ thresholds and the $3s \rightarrow 2p$ emission, are, respectively, $\boldsymbol{\epsilon}\cdot\mathbf{r}$ and $\boldsymbol{\epsilon}'^{*}\cdot\mathbf{r}$, with $\boldsymbol{\epsilon}$ and $\boldsymbol{\epsilon}'$ as polarization vectors. We adopt the most general geometrical setup, as shown in Fig. 1, where three coordinate systems are introduced. Two are related to the incident (xyz) and emitted $(x'y'z')$ photons, where z and z' axes are parallel to the propagation directions, forming ϑ and ϑ' angles $(0 \leqslant \vartheta, \vartheta' \leqslant \pi)$ with the magnetization **M**. The other $(x''y''z'')$ is associated with the sample and has z'' parallel to **M**, which is the quantization direction of the system. The angles φ and φ' $(0 \leqslant \varphi, \varphi' < 2\pi)$ of the incidence and the emission directions around **M** are taken with respect to x''.

Writing the scalar products in spherical coordinates $\boldsymbol{\epsilon}\cdot\mathbf{r} = r\Sigma_q (-1)^q \epsilon_{-q} C_q^{(1)}(\hat{r})$ and considering that $(\boldsymbol{\epsilon}^*)^q = \epsilon_q^*$ and $\epsilon^q = (-1)^q \epsilon_{-q}$, Eq. (1) can be put in the form

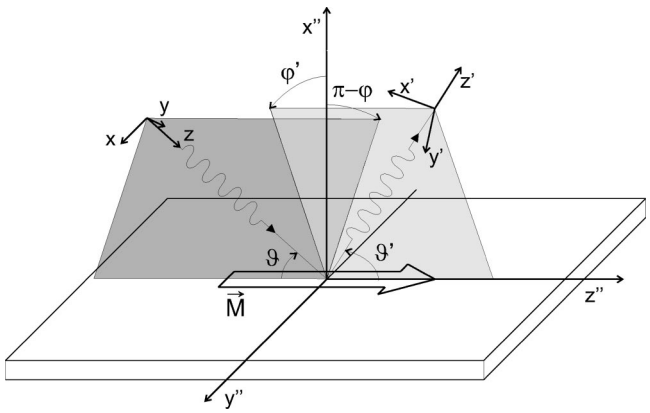

FIG. 1. Three coordinate systems required to describe the geometry of the scattering process. Two are related to the incident (xyz) and emitted $(x'y'z')$ photons; the other $(x''y''z'')$ is associated with the sample and has z'' parallel to **M**. x'' and y'' are supposed to be parallel to the octahedron axes in the case O_h crystal field.

$$\frac{d^2\sigma^{\epsilon\epsilon'}}{d\Omega' d(\hbar\omega')} = \sum_{|f\rangle} \left| \sum_{qq'} (-1)^{q'} \epsilon_q (\epsilon'_{-q'})^* \sum_{|n\rangle} \times \frac{\langle i|rC_q^{(1)}(\hat{r})|n\rangle\langle n|rC_{q'}^{(1)}(\hat{r})|f\rangle}{E_i - E_n + \hbar\omega + i\Gamma_n/2} \right|^2 \times \delta(E_i - E_f + \hbar(\omega - \omega')), \quad (2)$$

where the spherical tensor operators $C_m^{(l)} = \sqrt{4\pi/(2l+1)}\,Y_{lm}$, with the spherical harmonics Y_{lm}, are expressed in the $(x''y''z'')$ coordinates. The matrix elements appearing in Eq. (2) can be written in the representation of electron coordinates: $|i\rangle$, $|n\rangle$, $|f\rangle$ are N-electron state functions of $r_1, r_2, \ldots, r_N$ and $rC_q^{(1)}(\hat{r})$ is the one-electron operator $\Sigma_j r_j C_q^{(1)}(\hat{r_j})$. We prefer an expression with the order of initial, intermediate, and final states from left to right in view of the following definitions of straightforward interpretation.[18] The expression of the polarization covariant components ϵ_q are obtained in terms of the Cartesian coordinates of different frames that are related through the rotation

$$\begin{pmatrix} x'' \\ y'' \\ z'' \end{pmatrix} = \begin{pmatrix} \cos\vartheta\cos\varphi & -\sin\varphi & \sin\vartheta\cos\varphi \\ \cos\vartheta\sin\varphi & \cos\varphi & \sin\vartheta\sin\varphi \\ -\sin\vartheta & 0 & \cos\vartheta \end{pmatrix} \begin{pmatrix} x \\ y \\ z \end{pmatrix}.$$

For circular polarizations one has

$$(\boldsymbol{\epsilon}^+)_q = \begin{cases} \frac{1}{2}(1-\cos\vartheta)e^{i\varphi}, & q=1 \\ -\frac{1}{\sqrt{2}}\sin\vartheta, & q=0 \\ \frac{1}{2}(1+\cos\vartheta)e^{-i\varphi} & q=-1, \end{cases}$$

$$(\boldsymbol{\epsilon}^-)_q=\begin{cases}-\frac{1}{2}(1+\cos\vartheta)e^{i\varphi}, & q=1\\ -\frac{1}{\sqrt{2}}\sin\vartheta, & q=0\\ -\frac{1}{2}(1-\cos\vartheta)e^{-i\varphi}, & q=-1,\end{cases}$$

where the definitions of polarization vectors

$$\boldsymbol{\epsilon}^+=\boldsymbol{\epsilon}^{Left}=-\boldsymbol{\epsilon}_1,$$

$$\boldsymbol{\epsilon}^-=\boldsymbol{\epsilon}^{Right}=\boldsymbol{\epsilon}_{-1}$$

have been adopted.[19] The same expressions hold also for the outgoing photon, as functions of ϑ' and φ'.

For the case where the polarization of the emitted beam is not measured, we have

$$\frac{d^2\sigma^{\epsilon}}{d\Omega' d(\hbar\omega')}=\sum_{|f\rangle}F^{\epsilon}(\hbar\omega)\,\delta(E_i-E_f+\hbar(\omega-\omega')),$$

where the square modulus in Eq. (2) has been developed as

$$F^{\epsilon}(\hbar\omega)=\sum_{\epsilon'}\sum_{q_1q_2q_3q_4}(-1)^{q_2+q_4}\boldsymbol{\epsilon}_{q_1}(\boldsymbol{\epsilon}'_{-q_2})^*(\boldsymbol{\epsilon}_{q_3})^*\times\boldsymbol{\epsilon}'_{-q_4}f_{q_1q_2}f^*_{q_3q_4}$$

with

$$f_{qq'}=\sum_{|n\rangle}\frac{\langle i|rC^{(1)}_q(\hat{r})|n\rangle\langle n|rC^{(1)}_{q'}(\hat{r})|f\rangle}{E_i-E_n+\hbar\omega+i\Gamma_n/2}. \tag{3}$$

For a straightforward interpretation of the results we focus on SO_2 symmetry, that of an isolated ion in a magnetic field. $|i\rangle$, $|n\rangle$, $|f\rangle$ are atomic $|\alpha JM\rangle$ states, where J is the total angular momentum quantum number, M its component along the quantization axis, and α includes all other quantum numbers. The selection rules allow only the transitions $M'=M+q$, so that only the $f_{q_1q_2}f^*_{q_3q_4}$ products with $q_1+q_2=q_3+q_4$ survive. To make the notation simpler we will refer to $F^{\epsilon}(\hbar\omega)$ hereafter; in order to have the cross section the further sum $\Sigma_{|f\rangle}F^{\epsilon}(\hbar\omega)\,\delta(E_i-E_f+\hbar(\omega-\omega'))$ is required. The results for $F^{sum}=F^+ + F^-$ and $F^{dich}=F^+-F^-$, the intensity for the sum and the difference over the incident photon circular polarizations, are

$$\begin{aligned}F^{sum}(\hbar\omega)=&(1+\cos^2\vartheta)(1+\cos^2\vartheta')S_1+(1+\cos^2\vartheta)\\&\times\sin^2\vartheta' S_2+\sin^2\vartheta(1+\cos^2\vartheta')S_3\\&+\sin^2\vartheta\sin^2\vartheta'[S_4+\mathrm{Re}\{S_5e^{2i(\varphi-\varphi')}\}]\\&+\sin 2\vartheta\sin 2\vartheta'[\mathrm{Re}\{S_6e^{i(\varphi-\varphi')}\}],\end{aligned} \tag{4}$$

$$\begin{aligned}F^{dich}(\hbar\omega)=&\cos\vartheta(1+\cos^2\vartheta')D_1+\cos\vartheta\sin^2\vartheta' D_2\\&+\sin\vartheta\sin 2\vartheta'[\mathrm{Re}\{D_3e^{i(\varphi-\varphi')}\}],\end{aligned} \tag{5}$$

where the terms

$$S_1=\frac{1}{4}(|f_{11}|^2+|f_{1-1}|^2+|f_{-11}|^2+|f_{-1-1}|^2),$$

$$S_2=\frac{1}{2}(|f_{10}|^2+|f_{-10}|^2),$$

$$S_3=\frac{1}{2}(|f_{01}|^2+|f_{0-1}|^2),$$

$$S_4=|f_{00}|^2,$$

$$S_5=\frac{1}{2}(f_{1-1}f^*_{-11}),$$

$$S_6=\frac{1}{4}(f_{10}f^*_{01}-f_{1-1}f^*_{00}-f_{00}f^*_{-11}+f_{0-1}f^*_{-10}),$$

$$D_1=\frac{1}{2}(-|f_{11}|^2-|f_{1-1}|^2+|f_{-11}|^2+|f_{-1-1}|^2),$$

$$D_2=-|f_{10}|^2+|f_{-10}|^2,$$

$$D_3=\frac{1}{2}(-f_{10}f^*_{01}+f_{1-1}f^*_{00}-f_{00}f^*_{-11}+f_{0-1}f^*_{-10})$$

depend on the incident photon energy $\hbar\omega$ through the functions $f_{qq'}$. In Eqs. (4) and (5) the angular dependence is made explicit and the atomic structure is entirely included in S_i and D_i coefficients: they are linear combinations of $f_{q_1q_2}f^*_{q_3q_4}$. For $(q_1,q_2)=(q_3,q_4)$ we have $|f_{q_1q_2}|^2$ terms, which contain sums of both diagonal and off-diagonal terms with respect to the intermediate states of the process. The diagonal terms involve the same intermediate state $|n\rangle$. The off-diagonal terms contain two different intermediate states $|n\rangle$ and $|m\rangle$ with the same symmetry properties: they are both reached with the same component of the transition operator, so that they have the same M, or more generally they belong to the same irreducible representation of the symmetry group of the system. The products $f_{q_1q_2}f^*_{q_3q_4}$ with $(q_1,q_2)\neq(q_3,q_4)$ are composed only of off-diagonal terms with intermediate states of different M. Usually the cross terms are smaller in magnitude than the diagonal ones, but they are not negligible,[20] especially in some particular geometries where they play an important role, as will be shown in Secs. III and V.

The total spectrum F^{sum} depends on a weighted sum of diagonal products through S_1, S_2, S_3, and S_4 and only through S_5 and S_6 from off-diagonal processes. The dichroic spectrum depends through D_1 and D_2 on the differences between $|f_{q_1q_2}|^2$ having different *magnetic quantum numbers* and also on the interference effects linked to the off-diagonal terms present in D_3. In general, the total and dichroic spectra are the sum of many products composed of an angular factor depending on ϑ, φ, ϑ', φ' and a spectral factor depending on ω, ω', so that a similar analytic form can be used for the structure of the energy-resolved spectra and for their integrals over $\hbar\omega_k$, $\hbar\omega_{k'}$, or both [giving $J(\vartheta,\varphi,\vartheta',\varphi')$].

III. THE ROLE OF THE INTERFERENCE

The development of the square modulus in Eq. (2) includes interference effects between the intermediate states, described by off-diagonal products, that are needed to obtain the most general angular dependence of the RIXS cross section. The φ and φ' dependence appears only if terms with $(q_1,q_2)\neq(q_3,q_4)$ are present, as can be seen from Eqs. (4) and (5). The dependence on $\varphi-\varphi'$ and not on φ and φ' separately comes from the symmetry of the magnetic ion. These terms have the form

$$\mathrm{Re}\{Xe^{ik(\varphi-\varphi')}\}=\mathrm{Re}\{X\}\cos[k(\varphi-\varphi')] - \mathrm{Im}\{X\}\sin[k(\varphi-\varphi')]$$

with $X=S_5$ for $k=2$ and $X=S_6,D_3$ for $k=1$. The presence of an antisymmetric part $(\sin[k(\varphi-\varphi')])$, in addition to a symmetric one $(\cos[k(\varphi-\varphi')])$, results in a change in the shape of F^{sum} and F^{dich} for inversion of $(\varphi-\varphi')$.

Thus the cross sections corresponding to specular configurations of the emission direction, with respect to the plane containing the magnetization and the incoming wave vector, are different. Such plane, which will be referred to as the $(\mathbf{k},\mathbf{M})$ plane, can be taken as the $x''z''$ plane (see Fig. 2), because in SO_2 symmetry all the planes containing $\mathbf{M}$ are equivalent. It is the presence of the magnetic interactions in the Hamiltonian of the system that breaks the mirror symmetry. As a consequence, the two half spaces for $y''>0$ and $y''<0$ are not equivalent.

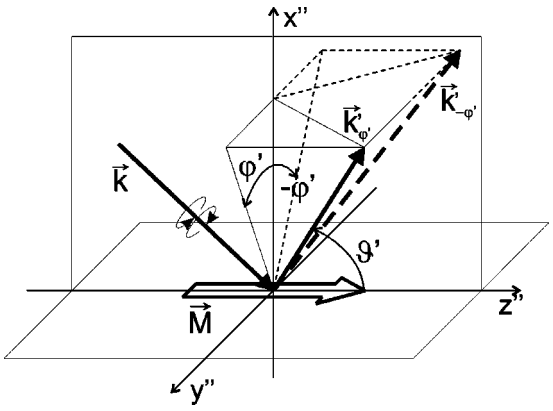

FIG. 2. Scattering geometry: in SO_2 symmetry we can choose the plane $x''z''$ as the $(\mathbf{k},\mathbf{M})$ plane. In the presence of magnetic interactions the emission direction symmetry with respect to this plane is broken. Thus the outgoing wave vectors $\mathbf{k}'(\vartheta',\varphi')$ and $\mathbf{k}'(\vartheta',-\varphi')$ are not equivalent.

This aspect is linked to the geometrical setup of the experiment and to the nature of the system: the antisymmetric part vanishes if the outgoing radiation is detected in the $(\mathbf{k},\mathbf{M})$ plane $(\sin[k(\varphi-\varphi')]=0)$ or if the electronic structure of the sample is such that $\mathrm{Im}\{S_5\}$, $\mathrm{Im}\{S_6\}$, $\mathrm{Im}\{D_3\}$ are zero. We investigate the problem in detail, because in the literature it has not been analyzed up to now, as most of the experiments were performed in the $(\varphi-\varphi')=0$ condition, i.e., with the magnetization in the scattering plane.[11,12]

To have a better insight, we look at the imaginary part of $f_{q_1q_2}f^*_{q_3q_4}$ products

$$\mathrm{Im}\{f_{q_1q_2}f^*_{q_3q_4}\}=-\frac{\overline{\Gamma}}{2}\sum_{|m\rangle|n\rangle}(E_m-E_n)\frac{\langle i|rC^{(1)}_{q_1}(\hat{r})|m\rangle\langle m|rC^{(1)}_{q_2}(\hat{r})|f\rangle\langle i|rC^{(1)}_{q_3}(\hat{r})|n\rangle\langle n|rC^{(1)}_{q_4}(\hat{r})|f\rangle}{[(E_i-E_m+\hbar\omega)^2+\overline{\Gamma}^2/4][(E_i-E_n+\hbar\omega)^2+\overline{\Gamma}^2/4]} \tag{6}$$

where the matrix elements $\langle a|rC^{(1)}_q(\hat{r})|b\rangle$ can be chosen as real for the magnetic ion and the lifetime has been fixed to the same value $\overline{\Gamma}$ for all intermediate states. From Eq. (6) we see that $\mathrm{Im}\{f_{q_1q_2}f^*_{q_3q_4}\}$ can be neglected with respect to $\mathrm{Re}\{f_{q_1q_2}f^*_{q_3q_4}\}$ if the multiplet structure of the intermediate configuration is such that the only states that interfere, i.e., with energy distance smaller than $\overline{\Gamma}$, are nearly degenerate with respect to $\overline{\Gamma}$ $(|E_m-E_n|\ll\overline{\Gamma})$. This condition strictly depends on the system in question and one cannot *a priori* know if it is fulfilled or not: numerical calculations of the multiplet structure of the intermediate configuration are required to make predictions on the possible observation of the mentioned asymmetry. $\mathrm{Im}\{f_{q_1q_2}f^*_{q_3q_4}\}\approx 0$ well out of the resonance or, of course, in the nonmagnetic case: the mirror symmetry of nonmagnetic crystals is thus recovered, as the Hamiltonian does not contain nonsymmetric terms. $\mathrm{Re}\{f_{q_1q_2}f^*_{q_3q_4}\}$ does not vanish in this case, so that the φ dependence still holds. These properties have been numerically checked using the approach exposed in Sec. IV. Further details are given in Sec. V.

Let us consider the two configurations shown in Fig. 3, where the beam directions in the first case (full arrows) are in specular positions with respect to the $x''y''$ plane (perpendicular to the magnetization) if compared to those in the second one (dashed arrows). The cross section for one of the two geometries with a given circular polarization of the incoming radiation coincides with that obtained for the other geometry with the opposite polarization. F^{sum} and F^{dich} are, respectively, symmetric and antisymmetric under such a reflection.

The discussed properties for F^{dich} [asymmetry for $(\varphi-\varphi')\rightarrow-(\varphi-\varphi')$ inversion and antisymmetry for $\vartheta,\vartheta'\rightarrow(\pi-\vartheta),(\pi-\vartheta')$ operation] imply that in the most general geometrical setup, when $\mathbf{k}$, $\mathbf{k}'$, $\mathbf{M}$ are not coplanar, reversing the incident beam polarization is not equivalent to reversing the magnetization direction (at variance with the

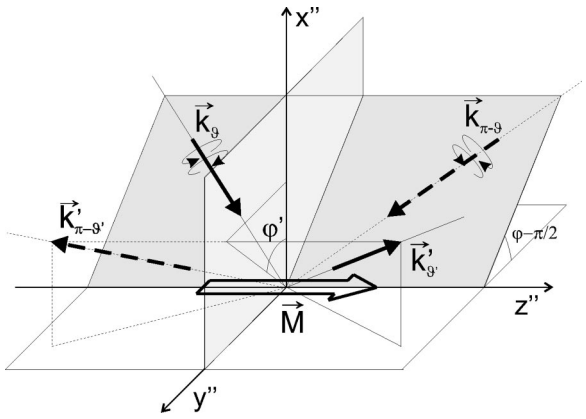

FIG. 3. Two configurations for the scattering geometry. The incoming and outgoing wave vectors for the second configuration are obtained by reflection with respect to the $x''y''$ plane. The reflection also changes the polarizations.

case with the magnetization in the scattering plane[8]). This can be easily understood in the case with the incoming beam normal to **M**. We notice in Fig. 4 that a π rotation of **M** causes a change in the half space where the photons are detected: moving the detection direction from the y'' positive half space to the negative one, or vice versa, implies a variation in the scattering probability, as we have previously discussed. This fact has to be considered when handling experimental data in order to prevent errors: the dichroism has to be measured by changing the polarization of the incident beam, as it is from its definition, and *not* by reversing the magnetization with the detection direction fixed in the laboratory frame.

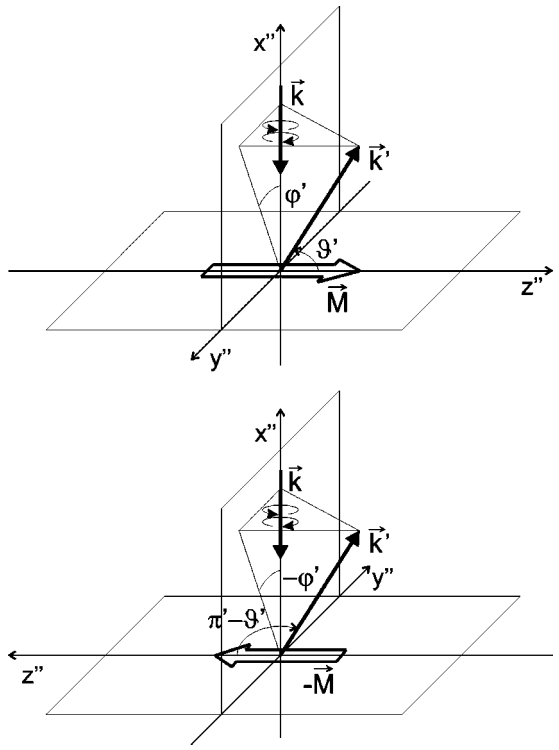

FIG. 4. Perpendicular geometry (the incoming beam direction is perpendicular to the magnetization). The reverse of the magnetization can be obtained by a rotation of π around the x'' axis, which keeps the system of axis of the right type. In the new coordinate system the direction of the wave vector $\mathbf{k}'$ varies from (ϑ', φ') to $(\pi - \vartheta', -\varphi')$.

IV. CALCULATION DETAILS

The numerical calculations have been done in the ionic approximation, using a single configuration all-electron picture. The matrix elements and the energy levels in Eq. (1) are calculated by the Hartree-Fock method with relativistic corrections.[21] The Slater integrals are rescaled to 80% (value commonly used in the literature) to take approximately into account the part of the intra-atomic correlation not included in the Hartree-Fock treatment. The crystal-field approach[22] has been adopted to simulate the solid-state environment of the ion. Octahedral symmetry has been considered. Band effects are not included, as in the ionic model they are assumed to be less important with respect to the multiplet structure in the calculation of the spectra in the L_3 region. This analysis corresponds to the case of a bulk atom in an ionic compound with an O_h geometry (where x'',y'',z'' are the octahedron axes and the crystal-field intensity is fixed to $10Dq = 1.0$ eV), with the addition of the magnetization parallel to z''.

The presence of a magnetization direction reduces the overall symmetry to C_{4h}. The three spherical components of the dipole operator belong to different representations of C_{4h}. Thus the expressions (4) and (5) obtained in SO_2 basis remain in the same form in the new crystal symmetry.[22,23] The atomic states $|JM\rangle$ redistribute into the irreducible representations of C_{4h} and the transition amplitudes between these states considerably changes. This argument applies also to the case of a tetragonal crystal field (T_d), provided the S_4 group, in place of C_{4h}, is used. The interatomic exchange interaction is simulated by applying a magnetic field H_{ex} coupled to spin moment only. It has been conventionally set to $\mu_B H_{ex} = 0.01$ eV: a quantitative description of the magnetic splitting is not required, because its effects on the spectral shape are much smaller compared with those coming from the electronic structure. The importance of the inclusion of the exchange interaction lies in the removal of the ground-state degeneracy and in the appropriate description of the symmetry of the initial state. The ground-state level ($^6S_{5/2}$ for Mn^{2+}, $^4F_{9/2}$ for Co^{2+}, $^3F_4$ for Ni^{2+}) is substituted by a manifold of equally spaced levels[24,25] with interlevel distance $\Delta E = g_S \mu_B H_{ex}$ where the Landé factor g_S is 1 for Mn^{2+}, 1/3 for Co^{2+} and 1/4 for Ni^{2+}. The energy width of the intermediate states (full width at half maximum) has been set to 0.4 eV (Mn^{2+}), 0.45 eV (Co^{2+}), and 0.5 eV (Ni^{2+}), in agreement with the L_3 core-hole lifetime.[26]

The finite temperature implies that the initial states $|i\rangle$ can be not only the ground state, but also some low-energy excited states populated at $T>0$. A weighted sum over the states of the initial configuration $1/Z\Sigma_{|i\rangle} e^{-(E_i - E_g)/k_B T}$ must be included in Eq. (2), where E_g is the ground-state energy, T is the temperature, and k_B the Boltzmann constant. At room temperature some magnetically split states, coming from a

single spectral term, can be populated. In this way the effect of the temperature will be taken into account introducing a temperature parameter $T_p = k_B T/\mu_B H_{ex}$.

V. PERPENDICULAR GEOMETRY

In this section we specialize the previous results to the case of the perpendicular geometry (propagation of the incident radiation along $-x''$), whose importance has been outlined in recent years, Refs. (8–11). Setting $\vartheta = \pi/2$ and $\varphi = \pi$, Eqs. (4) and (5) become

$$F^{sum}(\hbar\omega_k) = [\Sigma_1 + \Sigma_2 \cos 2\varphi' + \Sigma_3 \sin 2\varphi'] + \cos 2\vartheta' [\Sigma_4 - \Sigma_2 \cos 2\varphi' - \Sigma_3 \sin 2\varphi'], \tag{7}$$

$$F^{dich}(\hbar\omega_k) = \sin 2\vartheta' [\Delta_1 \cos\varphi' + \Delta_2 \sin\varphi'], \tag{8}$$

where

$$\Sigma_1 = \frac{1}{2}(3S_1 + S_2 + 3S_3 + S_4),$$

$$\Sigma_2 = \frac{1}{2}\mathrm{Re}\{S_5\},$$

$$\Sigma_3 = \frac{1}{2}\mathrm{Im}\{S_5\},$$

$$\Sigma_4 = \frac{1}{2}(S_1 - S_2 + S_3 - S_4),$$

$$\Delta_1 = -\mathrm{Re}\{D_3\},$$

$$\Delta_2 = -\mathrm{Im}\{D_3\}.$$

The main feature of the perpendicular geometry is that the dichroic signal is no more depending on differences among terms of the type $|f_{q_1 q_2}|^2$, as D_1 and D_2 terms are multiplied by $\cos\vartheta = 0$. The dichroism is only due to the interference between different excitation-emission paths described by the D_3 term. Differently from absorption, which in perpendicular geometry has no dichroism, in the scattering experiment we can observe a dichroic signal if we do not integrate on the emission angles.[11]

This geometry is compatible with the presence of an antisymmetric contribution, with reference to the φ' dependence, both in F^{sum} and in F^{dich}, due to the presence of $\sin 2\varphi'$ and $\sin\varphi'$ in Eqs. (7) and (8). The terms related to the interference processes cannot be neglected when performing analytic or numerical calculations, even if they are supposed to be smaller than the diagonal ones: there are experimental conditions where they play a crucial role. Two kinds of interesting geometrical setups will be considered and analyzed in detail, after a discussion of a simple exemplar case where only an ingredient contributes to dichroism and anisotropy.

In what follows we will present for RIXS in perpendicular geometry the analysis of the angular dependence of the integrated intensities, in the same spirit of the detailed work of Ref. 27 that was at the beginning of the quantitative analysis of x-ray absorption.

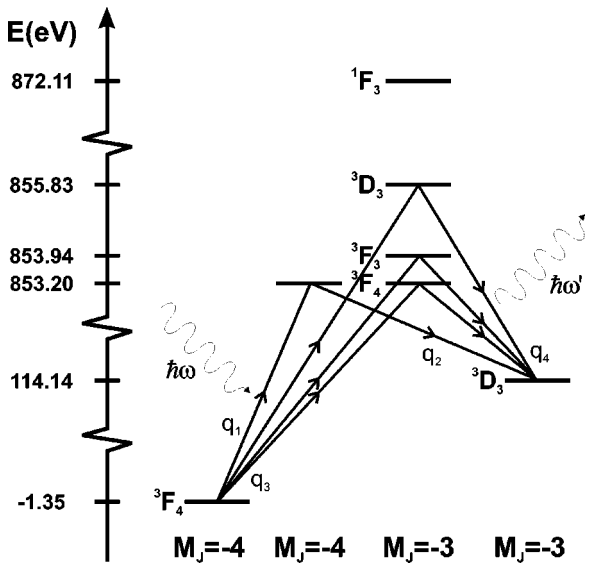

FIG. 5. Different absorption-emission paths contributing to $f_{0-1} f^*_{-10}$ term for Ni^{2+} $3d^8 \rightarrow 2p^5 3d^9 \rightarrow 3s^1 3d^9$ transitions (Ref. 18) in SO_2 symmetry at $T = 0$ K.

A. A simple case: Ni^{2+}

In analogy with the literature of the early 1990s on the study of absorption dichroism in term of ionic multiplets,[25] we report in detail the example of RIXS from a transition-metal ion at $T = 0$, in the limit of negligible crystal field (SO_2 symmetry), which can be almost calculated manually. We discuss the case of Ni^{2+} ($3d^8 \rightarrow 2p^5 3d^9 \rightarrow 3s^1 3d^9$) in the perpendicular geometry. From numerical calculations it is possible to estimate the relative weight of $\mathrm{Re}\{f_{q_1 q_2} f^*_{q_3 q_4}\}$ and $\mathrm{Im}\{f_{q_1 q_2} f^*_{q_3 q_4}\}$, directly connected to the absence of the $(\mathbf{k},\mathbf{M})$-plane mirror invariance discussed in Sec. III.

Let us have a look in Fig. 5 at the spectral terms of Ni^{2+}. The ground-state level in SO_3 symmetry is $^3F_4$. The lowest level of this term after magnetic splitting has $M_J = -4$. In the intermediate configuration manifold, only a few of the 60 states can be reached in dipole approximation: the lowest values of M_J are -4 and -3, arising, respectively, from $^3F_4$ and $^3F_3$, $^3D_3$, $^1F_3$.

The final states can only have $M_J = -3$ or $M_J = -2$ since there are no states with $M_J = -4$. As a consequence, if $q_1 = 0$ we can consider only the terms with $q_2 = -1$; if $q_1 = -1$ only those with $q_2 = 0$ or $q_2 = -1$ in $f_{q_1 q_2}$. Thus there are no interference terms in F^{sum}, while F^{dich} reduces to

$$F^{dich} = -\tfrac{1}{2}\sin 2\vartheta' [\cos\varphi' \mathrm{Re}\{f_{0-1} f^*_{-10}\} + \sin\varphi' \mathrm{Im}\{f_{0-1} f^*_{-10}\}].$$

Let us calculate f^*_{-10} and f_{0-1} with $|i\rangle = |3d^8, {}^3F_4, M_J = -4\rangle$ as initial state and $|f\rangle = |3s^1 3d^9, {}^3D_3, M_J = -3\rangle$ as fi-

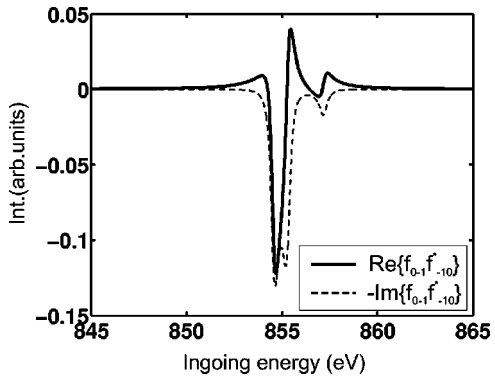

FIG. 6. $\mathrm{Re}\{f_{0-1}f^*_{-10}\}$ and $\mathrm{Im}\{f_{0-1}f^*_{-10}\}$ for Ni^{2+} in SO_2 symmetry at $T=0$ K, as a function of the incident photon energy. The dependence on the emission energy is trivial, because there is one possible final state.

nal state. The intermediate states for the two functions are indicated in Fig. 5.

We can see that for this system, with $\Gamma=0.5$ eV and the energy spread of the intermediate configuration multiplet of the order of 3 eV, $\mathrm{Re}\{f_{0-1}f^*_{-10}\}$ strongly oscillates and the peaks associated with different levels distant more than Γ can be distinguished in $\mathrm{Im}\{f_{0-1}f^*_{-10}\}$ (Fig. 6). The imaginary part has a strong contribution and the dichroic signal is dominated by φ' asymmetry. It is worth noticing that far from the resonance $\mathrm{Im}\{f_{0-1}f^*_{-10}\}\approx 0$ while $\mathrm{Re}\{f_{0-1}f^*_{-10}\}$ is still finite. In the tail region the imaginary part is negligible independently of the multiplet structure and no asymmetry in this low signal region can be found.[28]

B. Conical scan

Let us consider the geometrical arrangement shown in Fig. 7, where the emission is detected along a direction that can rotate around the incident one describing the surface of a cone with half aperture α and axis **k**.

This geometry is particularly useful for two reasons.

(i) RIXS measurements, especially in the soft x-ray range, are heavy influenced by self-absorption, which varies considerably with the angle between the scattering direction and the sample surface.[14] The self-absorption is constant along the conical scan and this configuration is particularly convenient.

(ii) The application of RIXS sum rules: the anisotropy of the energy integrated intensity $J^{sum}_{\perp}$ ($\perp$ recalls the perpendicular geometry of incident light) is linked to a linear combination of multipole moments of the system of second and fourth order only. This implies that once α has been fixed, $J^{sum}_{\perp}$ is modulated as a function of β and the amplitude of the modulation can give information on the quadrupolar and hexadecapolar moments of the charge and magnetic densities of the partially filled shells in the initial state.[15,28]

The angles for the description of the results are now α and β, functions of the angles ϑ' and φ' that have been used so far. We have

$$F^{sum}(\hbar\omega_k)=A(\alpha)+B(\alpha)\cos 2\beta+I_s(\alpha)\sin\beta, \qquad (9)$$

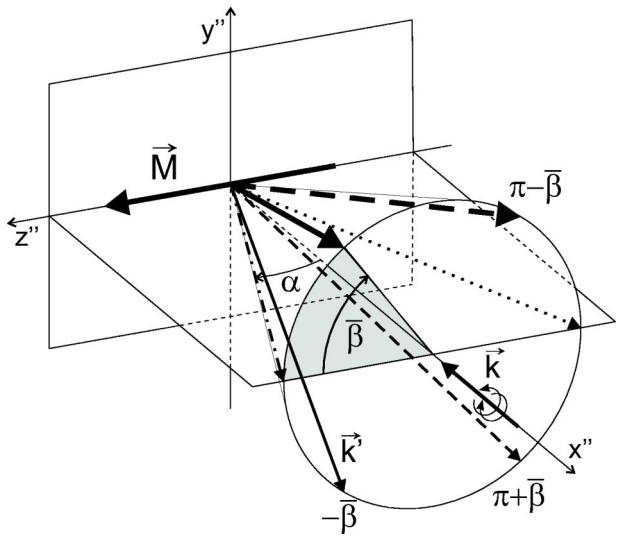

FIG. 7. Geometry configuration of the calculation shown in the present paragraph. A scan of the emission direction around the cone with **k** axis and half aperture $\alpha=45°$ has been performed. The relation between the angles in the various cases has been outlined. In the numerical calculations presented in this paper $\bar{\beta}=45°$. Each line style of $\mathbf{k}'$ has a corresponding spectrum in Figs. 8, 9, and 10.

$$F^{dich}(\hbar\omega_k)=R_d(\alpha)\cos\beta+I_d(\alpha)\sin 2\beta, \qquad (10)$$

where

$$A(\alpha)=(\Sigma_1-\Sigma_2)+(3\Sigma_2-\Sigma_4)\cos^2\alpha,$$

$$B(\alpha)=(\Sigma_2+\Sigma_4)\sin^2\alpha,$$

$$I_s(\alpha)=2\Sigma_3\sin 2\alpha,$$

$$R_d(\alpha)=\Delta_1\sin 2\alpha,$$

$$I_d(\alpha)=\Delta_2\sin^2\alpha.$$

The coefficients depending only on the imaginary part of nondiagonal products $\mathrm{Im}\{f_{q_1q_2}f^*_{q_3q_4}\}$ have been called $I_{s,d}$. Thus the deviation of the β plot of F^{sum} from the $\cos 2\beta$ profile and that of F^{dich} from $\cos\beta$ shape reveals the importance of these features.

All the symmetry properties and angular dependence that have been discussed in Sec. III are contained in Eqs. (9) and (10). The dichroism is reversed for a reflection of the emission direction with respect to $x''y''$ plane, which changes β into $180°-\beta$, while F^{sum} is left unaffected. An asymmetry is found for reflections with respect to the $x''z''$ plane for both F^{sum} and F^{dich}. This effect is related to the presence of I_s and I_d, i.e., the imaginary part of the nondiagonal products $f_{q_1q_2}f^*_{q_3q_4}$. If no asymmetry is found experimentally, then I_s and I_d are negligible compared with $B(\alpha)$ and $R_d(\alpha)$ and the results, as far as the angular dependence of the integrated cross section is concerned, are similar to the ones evaluated neglecting the differences between the intermediate state eigenvalues in the energy denominators of Eq. (3).[6,28]

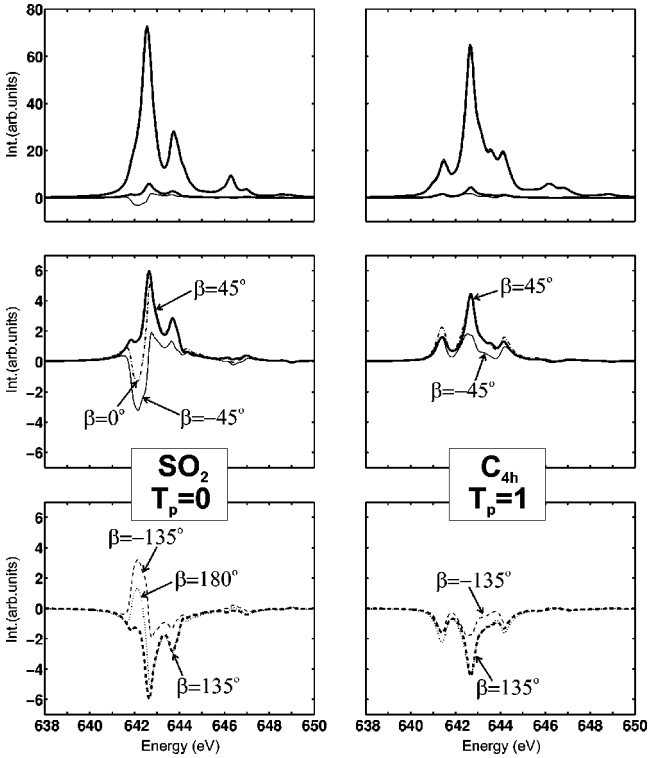

FIG. 8. RIXS total and dichroic spectra of Mn^{2+} in the L_3 region as functions of the incident photon energy, after the integration over the $3s \rightarrow 2p$ decay channel. On the left panels the SO_2 symmetry case at 0 K is presented; on the right panels a $10Dq = 1.0$ eV octahedral crystal field and a finite temperature have been introduced. In the top panels the total signal for $\beta = 45°$ and $\beta = -45°$ (almost indistinguishable) are compared with the dichroic signal, which is magnified in the other panels. The line styles of the curves correspond to those of Fig. 7: dash-dotted (dotted) for $\beta = 0°$ (180°); thick (thin) straight for $\beta = 45°$ ($-45°$); thick (thin) dashed for $\beta = 135°$ ($-135°$).

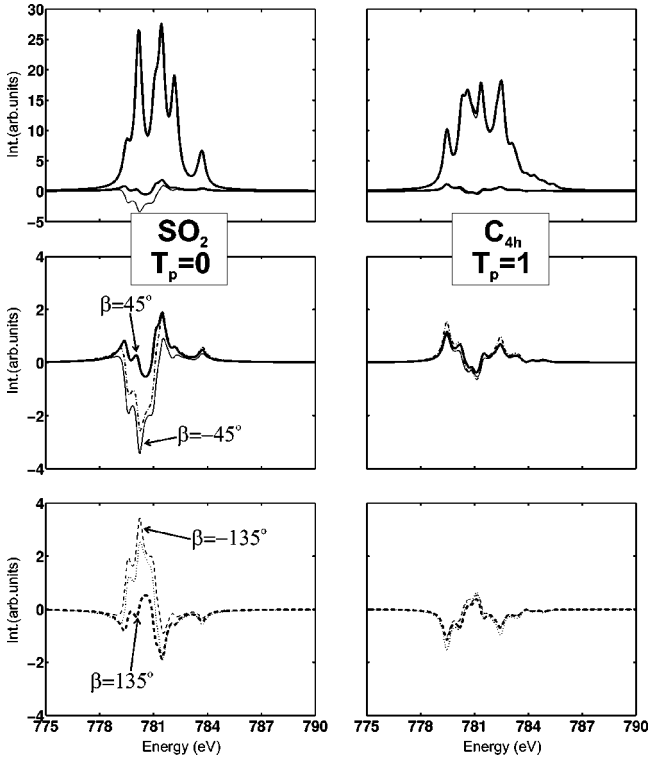

FIG. 9. RIXS total and dichroic spectra of Co^{2+} for the scattering geometry depicted in Fig. 7. For further details see the caption of Fig. 8.

The numerical calculations of the RIXS total signal and dichroism for Mn^{2+}, Co^{2+}, and Ni^{2+} are presented for the case $\alpha = 45°$ (the angle giving the maximum dichroism intensity). The total signal is compared to the dichroic one at $\beta = \pm 45°$ and the dichroism intensity is given at $\beta = 0°$, $\pm 45°$, $\pm 135°$, 180° (corresponding to $\bar{\beta} = 45°$ in Fig. 7). The spectra are integrated over the emitted photon energy (in analogy to the integrated resonant Raman scattering experimental measurements of Ref. 15).

The spectra in the left part of Figs. 8, 9, and 10 are associated to the ions in cylindrical symmetry at $T = 0$. In the upper part we compare the total and dichroic signals at $\beta = \pm 45$ on the same scale. The excitation corresponds to the L_3 region only. L_2 shows no dichroism as pointed out also in other works.[8,9,15] The properties of the dichroism are displayed in the other panels on a magnified scale: it changes sign passing from $\bar{\beta}$ to $\pi - \bar{\beta}$, as can be seen comparing the left and the right panels in Figs. 8, 9, and 10; the spectra for $\bar{\beta}$ and $-\bar{\beta}$ look quite different: the antisymmetric term in Eq. (8), linked to $\mathrm{Im}\{D_3\}$, is not negligible. The inclusion of a cubic crystal field ($10Dq = 1.0$ eV) and of the temperature ($T_p = 1$) considerably changes the shape of the spectra (right

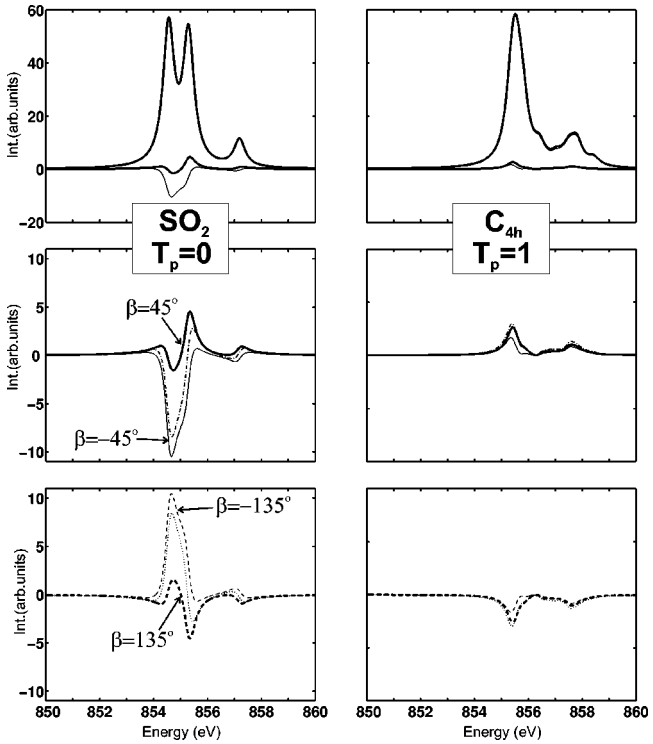

FIG. 10. RIXS total and dichroic spectra of Ni^{2+} for the scattering geometry depicted in Fig. 7. For further details see the caption of Fig. 8.

panels of Figs. 8, 9, and 10) with respect to the isolated ion in $M=-J$ ground state. Both the effects have different physical origins, but they are treated together in this analysis, as they have the same quenching effect on the asymmetry with respect to $\beta \rightarrow -\beta$ transformation.

This is not completely true in Mn^{2+}, where the difference between the $\overline{\beta}$ and $-\overline{\beta}$ curves is still appreciable: the high value of g_S results in a larger splitting among the levels originated by the ground state than in the cases of Ni^{2+} and Co^{2+}; thus the thermal energy is equal to the magnetic splitting and very few of the excited levels are populated. Moreover, its excited configuration with four holes in the $3d$ valence shell and a core hole in the $2p$ shell results in a multiplet structure with 1260 states, most of them being very close in energy, producing considerable interference effects, giving rise to relevant contributions of the off-diagonal products. The effect of the crystal field is decreased on Mn^{2+} ions, having no orbital moment: the ${}^6S_{5/2}$ ground state is not modified by the octahedral field. The spectra obtained by summing the two incident beam polarizations, given in the upper panel, show a weak β dependence. In fact, only few terms contain φ' in the cross section (7) and their weight is overwhelmed by the other terms, composed by a much greater number of processes: Σ_1, $\Sigma_4 \gg \Sigma_2$, Σ_3. In particular, in SO_2 symmetry $f_{1-1}f^*_{-11}=0$ for Ni^{2+}, so that F^{sum} is φ' independent. These effects on φ' dependence are transferred to the β dependence.

The β dependence of the scattering cross section integrated over the incident photon energy (the L_3 edge), as well as the emitted one, has been also studied. This quantity that results from the contribution of different spectral features has not necessarily stronger angular dependence than the single structures, but is considered as an interesting experimental output in view of the application of the RIXS sum rules. Only one case is present in the literature analyzing Co^{2+} integrated intensity of the dichroic signal.[15] Our calculation has been performed on the same systems and with the same calculation parameters as the previous one. A larger number of β angles has been investigated. The resultant plots are reported in Figs. 11 and 12 for Mn^{2+} and Co^{2+}. In the left column we give the results obtained in SO_2 symmetry at $T_p=0$. The sum and the difference of the intensities on the incident polarizations are given in the upper panel: the relative magnitude of the dichroism can be easily inferred. The central panels with enlarged scale allow an easier view of their shape. The dots represent the values coming from the full numerical calculations and the lines are the fitting functions given by Eqs. (9) and (10). The departure of the anisotropic part of $J_\perp^{sum}$ from the $\cos 2\beta$ shape gives the idea of the weight of the imaginary part of the nondiagonal products. It is caused by a $\sin\beta$ term, producing a raising and a lowering of the 90° and 270° minima, respectively, and resulting in an asymmetry with respect to the 180° line, which divides the plot in the same way as the $(\mathbf{k},\mathbf{M})$ plane does. The fit of the numerical data allows a quantitative determination of this effect, given by the ratio I_s/B. Analogously, the importance of a full description of the interference can be seen from the deviation of $J_\perp^{dich}$ from the $\cos\beta$ trend. It is due to the $\sin 2\beta$ term, increasing the number of maxima, minima, and nodes of the dichroism. It is also responsible for the presence of the maximum of $J_\perp^{dich}$ out of the $(\mathbf{k},\mathbf{M})$ plane. The $R_d(\alpha)\cos\beta + I_d(\alpha)\sin 2\beta$ fit of the numerical data determines the I_d/R_d ratio, which is a measure of the asymmetry of the dichroic signal with respect to the $(\mathbf{k},\mathbf{M})$ plane. The values used in these fits are listed in Table I.

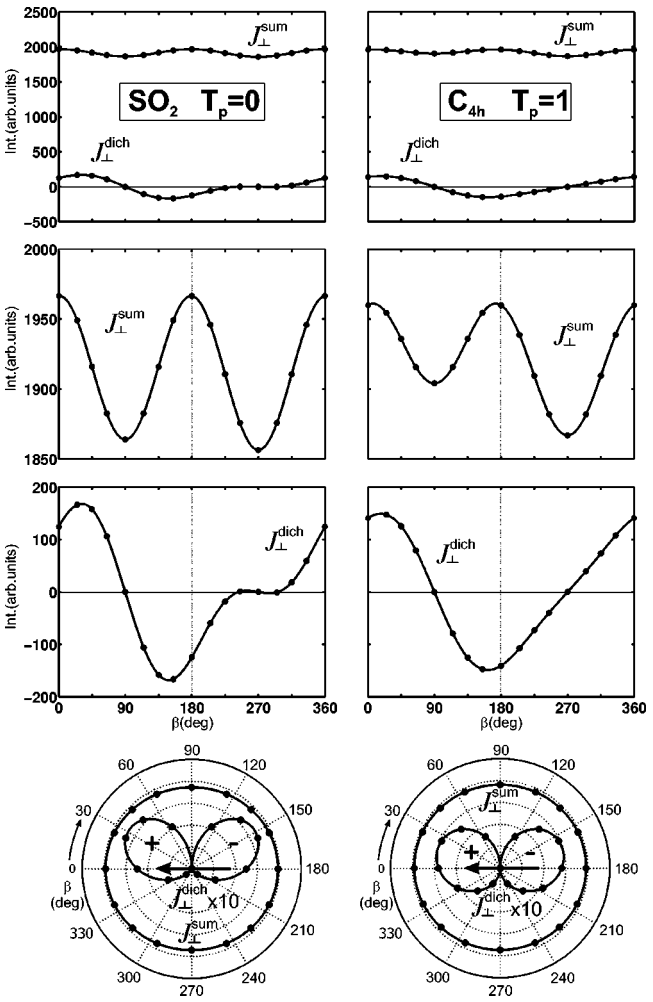

FIG. 11. Integrated scattering intensity for Mn^{2+} as a function of β, for the case $\alpha=45°$. The dots are the results of the numerical calculations and the straight lines are the fits.

In the absence of crystal field and for $T_p=0$, $J_\perp^{sum}$ is nearly symmetric. This is not the case for $J_\perp^{dich}$, because it is entirely given from nondiagonal products, with imaginary part comparable to the real part. The size of the asymmetry can be straightforwardly grasped from the bottom panel, containing the polar plot of $J_\perp^{sum}$ and $J_\perp^{dich}$ (the latter multiplied by a factor 10). It can be easily seen that the former is nearly symmetric at variance with the latter.

The right columns report the panels corresponding to the case of C_{4h} symmetry at $T_p=1$. It is worth noticing that the introduction in the Hamiltonian of a term where y'' and z'' are equivalent directions makes $J_\perp^{sum}$ more isotropic. The amplitude of its oscillations mainly given to B/A is reduced and the polar trend changes from ovoidal to nearly circular. $J_\perp^{dich}$ becomes more symmetric: it changes from a four-lobe but-

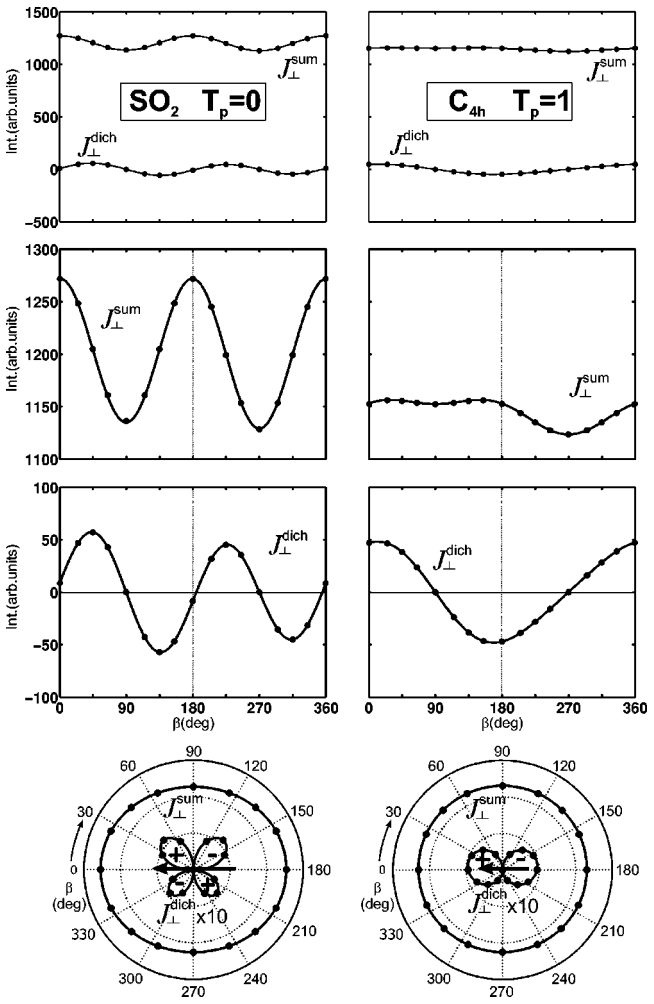

FIG. 12. Integrated scattering intensity for Co^{2+} as a function of β, for the case $\alpha=45°$. The dots are the results of the numerical calculations and the straight lines are the fits.

terfly shape, with different size for adjacent lobes, to a two-lobe structure more similar to a $\cos\beta$ shape. The dichroism intensity is also reduced by the increase of the temperature.

To make more evident the separate effects of the crystal field and of the finite temperature we give more plots for the case of Ni^{2+}, the simple case discussed before. In Fig. 13 on the four columns there are, respectively, the results for SO_2 symmetry at $T_p=0$, SO_2 symmetry at $T_p=1$, C_{4h} symmetry at $T_p=0$, and C_{4h} symmetry at $T_p=1$. The sequence of the panels in different rows is the same as in Figs. 11 and 12. The butterfly shape for $J_\perp^{dich}$ of the free ion at $T_p=0$ has the same pattern of the signs of the four lobes with respect to the previous cases, but the two lobes at high β values are more pronounced. As a result the dichroic signal at $\beta=0°$ is negative. One has to note that this characteristic is a consequence of the integration on incoming energy; this is not true for all the features of $F_\perp^{dich}(\hbar\omega_k)$. The increase of the temperature in the free ion case makes $J_\perp^{sum}$ plot evidently circular and creates a two-lobe structure for $J_\perp^{dich}$ with the maximum around $\beta=25°$. If we consider the case where the temperature is still zero but the crystal field has been turned on we can observe similar effects in the shape of both signals. The maximum of the dichroism is in the same position but is much larger. The combined effect of crystal field and finite temperature is visible in the last column: the shape of the dichroic signal is the same but with the maximum at $\beta\approx15°$. The shift of the maxima of the lobes from high β values, for the case corresponding to SO_2 symmetry at $T_p=0$, to low β values, for the case $T_p=1$, comes from the contribution of the paths starting from the lowest excited state. This shift is observed also with the inclusion of the crystal field at $T_p=0$. In fact, by increasing the octahedral field, the states in the d^8 manifold of the type $^{2S+1}L_J=\ ^3F_4$ rearrange and a crossing between the ground state and the lowest excited state occurs when the crystal and the exchange fields are of the same size.

The combined effect of the crystal field and of the finite temperature gives rise to the replacement of the original butterfly shape with a distorted 8-like form that moves towards, without reaching it, the perfect $\cos\beta$ trend for $J_\perp^{dich}$.

The only experimental result concerning β plots of the dichroic signal is that of Ref. 15 obtained for a cobalt compound. In that paper there is no evidence of any $\sin\beta$ type asymmetry of the dichroic signal. We must mention two remarks. The data were collected assuming that the reversal of the magnetization is equivalent to the reversal of the polarization of the incoming beam. This implies a $+\beta$ and $-\beta$ average of the outgoing radiation direction, which cancels out the possible antisymmetric terms in Eqs. (9) and (10). Furthermore, the nature of the Co ferrite sample used, composed of a majority of octahedral and a minority of tetrahedral sites in antiferromagnetic coupling,[29] probably would have critically hidden any possible asymmetry.

A direct check of detectable asymmetric contributions in a low-temperature experiment and using a system with low crystal-field effects would be of interest for future experimental work.

TABLE I. Values of the parameters appearing in Eqs. (9) and (10) used for the fit of the numerical data of the β plots.

	Mn^{2+}		Co^{2+}		Ni^{2+}	
	SO_2 $T_p=0$	C_{4h} $T_p=1$	SO_2 $T_p=0$	C_{4h} $T_p=1$	SO_2 $T_p=0$	C_{4h} $T_p=1$
A	1913	1923	1202	1145	4271	3851
B	53	37	70	8	574	20
I_s	4	19	4	14	0	68
R_d	125	141	9	47	−85	203
I_d	70	26	51	5	260	20

C. Coplanar geometry

Most of the few experiments in perpendicular geometry have been performed with the wave vectors of the incoming and outgoing photons and the magnetization of the sample in the same plane ($\varphi'=0$). Then Eqs. (7) and (8) assume simpler forms:

$$F^{sum}(\hbar\omega_k)=[\Sigma_1+\Sigma_2]+\cos 2\vartheta'[\Sigma_4-\Sigma_2], \qquad (11)$$

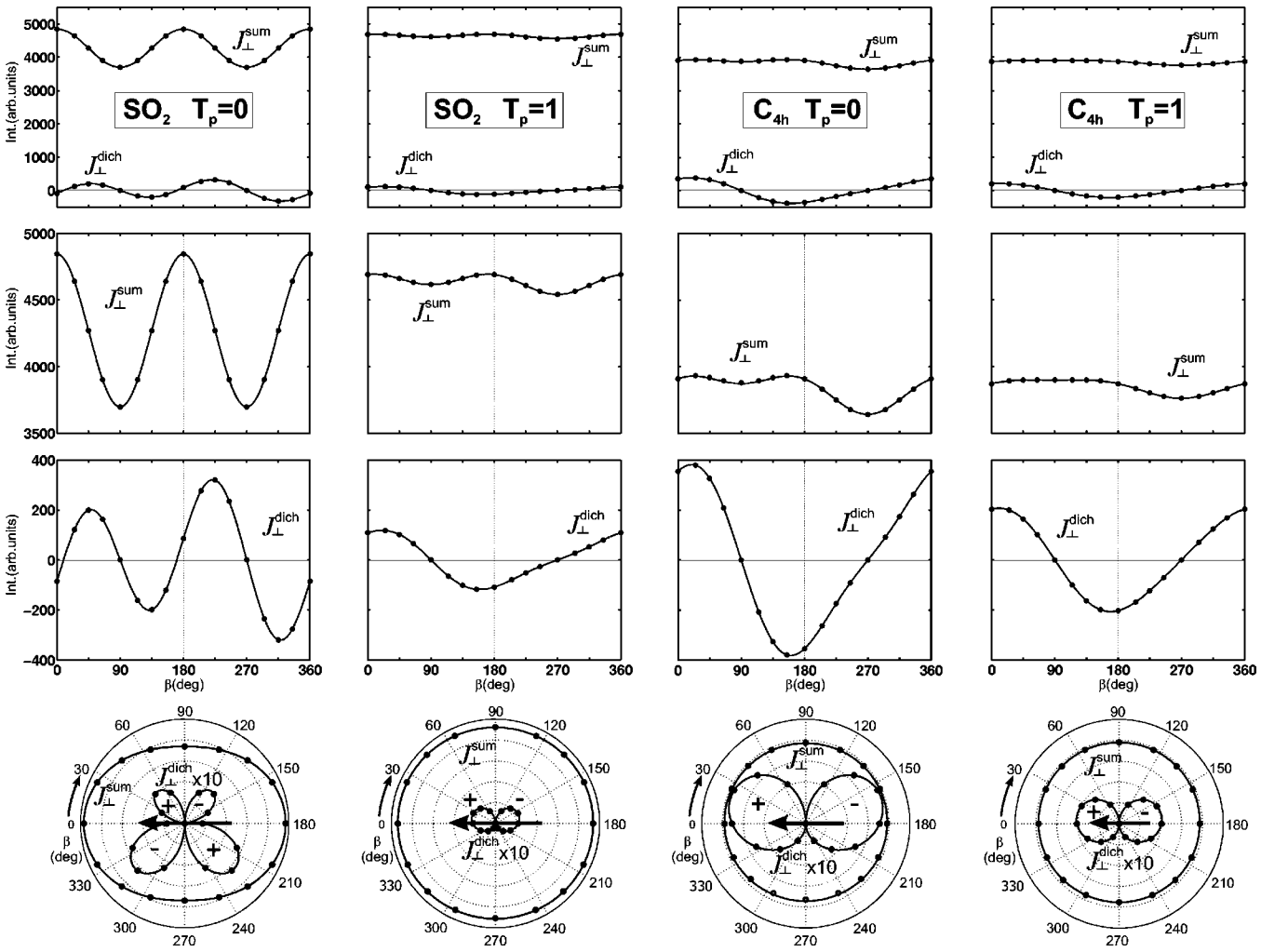

FIG. 13. Integrated scattering intensity for Ni^{2+} as a function of β, for the case $\alpha=45°$. The dots are the results of the numerical calculations and the straight lines are the fits.

$$F^{dich}(\hbar\omega_k)=\Delta_1 \sin 2\vartheta'. \tag{12}$$

The dependence on the emission angle of the signal summed on the ingoing photon polarizations is given by an isotropic part and a $\cos 2\vartheta'$ term, resulting in an elliptical shape. The dichroism is a $\sin 2\vartheta'$ function, showing thus a maximum for $\vartheta'=\pi/4$ and being zero at normal ($\vartheta'=0$) and backscattering ($\vartheta'=\pi/2$) directions. This ϑ' dependence has been observed on Co metal and Co ferrite systems for the RIXS intensity integrated over the incident and emitted photon energies, in the L_3 peak and the $3s\rightarrow 2p$ decay ranges.[13] The strong difference observed in such itinerant and localized samples for $J_\perp^{sum}$ highlights the role of RIXS as a probe of the atomic properties.

Some calculations of the angular dependence of the integrated scattering cross section $J_\perp(\vartheta')$ are presented here. The angular dependence is displayed in the polar plots shown in Fig. 14, relative to Mn^{2+}, Co^{2+}, and Ni^{2+} in a cubic crystal field of $10Dq=1.0$ eV, for different values of T_p. The calculated integrated intensities $J_\perp^{sum}$ and $J_\perp^{dich}$ (dots) follow the trend of the functions (11) and (12) (solid lines), whose fit to the calculations gives the parameters shown in Table II.

The anisotropy of $J_\perp^{sum}$ is related to the ground-state properties of the scatterer atom, as outlined in Ref. 13: it gives an estimation of the zeroth- and second-order moments. The anisotropy does exist even in the absence of the quadrupole moments and a perfectly circular trend implies the compensation of the two contributions. The effect of the temperature favors the backscattering emission ($\vartheta=90°$) in $J_\perp^{sum}$ and reduces the dichroism intensity. The sign of the dichroism intensity is positive in the range $0<\vartheta'<90°$ also in the case of Ni^{2+}, as in Co^{2+} and Mn^{2+}, if the crystal-field corrections are present.

VI. CONCLUSIONS

We have presented a study of the angle and polarization dependent RIXS cross section for magnetic materials with circular polarization of the incident light and assuming that the emitted radiation is collected without control of the polarization but as a function of the outgoing direction, varying in the full range of half solid angle. The formalism (in analogy with the theoretical work on absorption[25,27] that allowed us to study the dichroism in $L_{2,3}$ edges, the line shapes

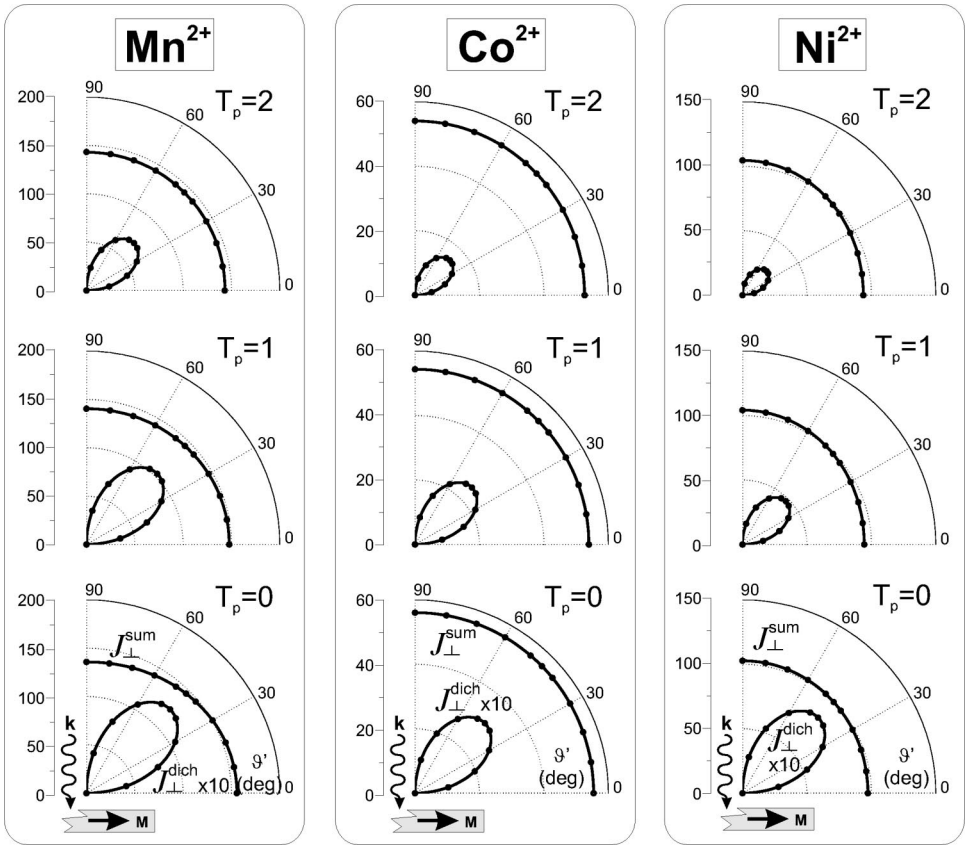

FIG. 14. Integrated scattering intensity $J_{\perp}^{sum}$ and $J_{\perp}^{dich}$, calculated for Mn^{2+}, Co^{2+}, and Ni^{2+} in perpendicular geometry with the emission direction in the (**k**,**M**) plane. $J_{\perp}^{sum}$ presents an ovoidal shape; $J_{\perp}^{dich}$, which has been amplified by a factor 10, follows a $\sin 2\vartheta'$ trend. The intensities are given in arbitrary units, comparable along each column. The curves for various values of T_p are given. The dots are the results of the numerical calculations and the straight lines are the fits.

in XAS spectra and the branching ratio) is based on ionic model, calculating the electron level multiplets and the transition matrix elements. We have obtained the full expression of the cross section, the sum and the difference of the incident photon polarizations as a function of the energies of the incoming and outgoing beams and their angles (ϑ,φ) and (ϑ',φ') with respect to the magnetization axis, pointing out the effect of the interference due to nondiagonal products of partial amplitudes $f_{q_1q_2}f^*_{q_3q_4}$, i.e., the interferences between different excitation-decay paths. The choice of the perpendicular geometry $(\vartheta=\pi/2,\varphi=\pi)$ of incoming beam[9,11] is particularly interesting as the dichroic signal is dependent exclusively on these nondiagonal interference terms. The line shapes as well as the integrated signals are particularly sensitive to the detailed description of the intermediate states, containing a core hole and a valence electron more than the ground state, as they are critically dependent on the interference terms. Additionally the final state effects associated with the $3s\rightarrow 2p$ inner shell decay contribute to the scattering cross section through the pattern of the available transition to the final multiplet.

TABLE II. Values of the parameters appearing in Eqs. (11) and (12) used for the fit of the numerical data of the ϑ' plots. The calculations are given in the same arbitrary units, so that the comparison among columns for the same element is significant. However, quantities in this table and Fig. 14 are not on the same scale as those in Table I and Figs. 11, 12, and 13.

	Mn^{2+}			Co^{2+}			Ni^{2+}		
$T_p\rightarrow$	0	1	2	0	1	2	0	1	2
$\Sigma_1+\Sigma_2$	143.1	142.0	141.3	55.7	54.1	53.3	100.0	99.3	99.1
$\Sigma_4-\Sigma_2$	7.1	2.1	−0.9	−0.3	−0.2	−0.7	−2.7	−4.9	−5.4
Δ_1	8.9	7.2	4.7	3.1	2.5	1.5	8.3	4.7	2.6

We have studied the total and dichroic signals in perpendicular geometry with a conical scan of the emission direction around the incidence one that has been recently proposed[15] in a novel experimental work. If the system is fully polarized (low temperature) and the effects of the crystal field are low (in the limit of SO_2 geometry), asymmetric patterns can be found (butterfly shape) for dichroism and also the total signal can have antisymmetric contribution with respect to the (**k**,**M**) plane. These effects are dramatically quenched by the rise of temperature and also by the contribution of crystal field, which is used to describe the crystalline environment in the ionic model. This particular shape should, however, be observable at low temperature. The polar scan with the emission direction $\mathbf{k}'$ in the (**k**,**M**) plane is also discussed. Here some experiments already exist and the shape of the dichroic signal as a function of ϑ' can be a careful test of the theory and strongly depends on the crystalline environment and temperature.

Finally we must point out that this work is based on a full calculation of the cross section (2) and the partial amplitudes $f_{q_1q_2}$ given by Eq. (3), without using any approximation hiding and averaging the structure of energy multiplets as well as the ω dependence of the spectra. Any approximation of this type would deeply affect the calculation of the nondiagonal products, missing the appropriate value of interference

effects between different absorption-emission paths which are responsible for the dichroism in perpendicular geometry.

The dichroic signal in a conical scan as well as in the planar geometry have been detected[9,15] in recent experimental work on angle-resolved RIXS at the $2p$ resonance and with the $3s \rightarrow 2p$ deexcitation channel. If the angular dependence of the integrated dichroic signal will be available or, even better, the dependence of the shape of the spectrum in ω as a function of the angle will be obtained, it would be possible to give a quantitative description of these effects in terms of the ground- and excited-state properties. The existence of dichroic signal in perpendicular geometry is a consequence of the interference between absorption-emission paths that, going from the same initial and final states, are passing through intermediate states of different magnetic numbers. The angular dependence of the dichroism in this geometry can also check the phases of this second-order partial amplitudes given by Eq. (3) and, in particular (if intermediate states with appropriate magnetic numbers exist), can induce an asymmetry with respect to the $(\mathbf{k},\mathbf{M})$ plane both in the dichroic and in the total signal.

We have seen that the simple and illuminating case of Ni^{2+} in cylindrical symmetry can be analytically discussed in a calculation that can be performed almost manually, once the appropriate energy structure and matrix elements have been computed. We think that this approach, avoiding approximations in the evaluation of the cross section, is the way to interpret accurately the outcome of the promising new experimental works.

ACKNOWLEDGMENTS

The authors are indebted to L. Braicovich, G. Ghiringhelli, C.R. Natoli, and A. Tagliaferri for fruitful discussions. This work was funded by INFM, within the research program for the theoretical and computational support to the use of synchrotron radiation.

*Electronic address: ferriani@unimore.it

[1] A. Kotani and S. Shin, Rev. Mod. Phys. **73**, 203 (2001).
[2] G. van der Laan, J. Electron Spectrosc. Relat. Phenom. **101-103**, 859 (1999).
[3] J. Luo, G.T. Trammel, and J.P. Hannon, Phys. Rev. Lett. **71**, 287 (1993).
[4] P. Carra, M. Fabrizio, and B.T. Thole, Phys. Rev. Lett. **74**, 3700 (1995).
[5] M. van Veenendaal, P. Carra, and B.T. Thole, Phys. Rev. B **54**, 16 010 (1996).
[6] F. Borgatti, G. Ghiringhelli, P. Ferriani, G. Ferrari, G. van der Laan, and C. M. Bertoni (unpublished).
[7] G. van der Laan and B.T. Thole, J. Phys.: Condens. Matter **7**, 9947 (1995).
[8] B.T. Thole, H.A. Dürr, and G. van der Laan, Phys. Rev. Lett. **74**, 2371 (1995).
[9] L. Braicovich, G. van der Laan, G. Ghiringhelli, A. Tagliaferri, M.A. van Veenendaal, N.B. Brookes, M.M. Chervinskii, C. Dallera, B.D. Michelis, and H.A. Dürr, Phys. Rev. Lett. **82**, 1566 (1999).
[10] L. Braicovich, G. van der Laan, G. Ghiringhelli, A. Tagliaferri, and N.B. Brookes, Phys. Rev. B **66**, 174435 (2002).
[11] K. Fukui, H. Ogasawara, A. Kotani, T. Iwazumi, H. Shoji, and T. Nakamura, J. Phys. Soc. Jpn. **70**, 1230 (2001).
[12] K. Fukui, H. Ogasawara, A. Kotani, T. Iwazumi, H. Shoji, and T. Nakamura, J. Phys. Soc. Jpn. **70**, 3457 (2001).
[13] A. Tagliaferri, Ph.D. thesis, Consorzio Politecnico di Torino—Politecnico di Milano, 1999.
[14] L. Braicovich, F. Borgatti, A. Tagliaferri, G. Ghiringhelli, N.B. Brookes, P. Ferriani, and C.M. Bertoni, Appl. Phys. A: Mater. Sci. Process. **73**, 679 (2001).
[15] L. Braicovich, A. Tagliaferri, G. van der Laan, G. Ghiringhelli, and N.B. Brookes, Phys. Rev. Lett. **90**, 117401 (2003).
[16] J.J. Sakurai, *Advanced Quantum Mechanics* (Addison-Wesley, Reading, MA, 1967).
[17] C. Cohen-Tannoudji, J. Dupont-Roc, and G. Grynberg, *Processus d'interaction Entre Photons et Atomes* (InterEditions/Editions du CNRS, Paris, 1988).
[18] To obtain Eq. (2) we have used the relation $(-1)^q \langle a|rC_q^{(1)}|b\rangle = \langle b|rC_{-q}^{(1)}|a\rangle$. Thus matrix-element magnetic selection rules read $M_b - M_a = -q$.
[19] J.D. Jackson, *Classical Electrodynamics* (Wiley, New York, 1975).
[20] F.M.F. de Groot, Phys. Rev. B **53**, 7099 (1996).
[21] R.D. Cowan, *The Theory of Atomic Structure and Spectra* (University of California Press, Berkeley, 1981).
[22] P.H. Butler, *Point Group Symmetry, Applications, Methods and Tables* (Plenum, New York, 1981).
[23] P. Carra and B.T. Thole, Rev. Mod. Phys. **66**, 1509 (1994).
[24] J.B. Goedkoop, B.T. Thole, G. van der Laan, G.A. Sawatzky, F.M.F. de Groot, and J.C. Fuggle, Phys. Rev. B **37**, 2086 (1988).
[25] G. van der Laan and B.T. Thole, Phys. Rev. B **42**, 6670 (1990).
[26] O. Keski-Rahkonen and M.O. Krause, At. Data Nucl. Data Tables **14**, 139 (1974).
[27] G. van der Laan and B.T. Thole, Phys. Rev. B **43**, 13 401 (1991).
[28] P. Ferriani, Ph.D. thesis, Università degli studi di Modena e Reggio Emilia, 2003.
[29] V.A.M. Brabers, in *Handbook of Magnetic Materials*, edited by K.H.J. Buschow (North-Holland, Amsterdam, 1995).